SCIENTIFIC REPORTS
nature research

Check for updates

OPEN

Effect of in situ VSi_2 and SiC phases on the sintering behavior and the mechanical properties of HfB_2-based composites

Soheil Ghadami[1]✉, Ehsan Taheri-Nassaj[1], Hamid Reza Baharvandi[2] & Farzin Ghadami[1]

In situ HfB_2–SiC–VSi_2 composite was fabricated by reactive pressureless sintering at the temperature of 2150 °C for 4 h under a vacuum atmosphere. In situ SiC and VSi_2 reinforcements were formed using VC and Si powders as starting materials according to the following reaction: VC + 3Si = SiC + VSi_2. Microstructural studies and thermodynamic calculations revealed that in situ VSi_2 and SiC phases were mostly formed and homogeneously distributed in HfB_2 skeleton. The results showed that the density of in situ HfB_2–SiC–VSi_2 composite was 98%. Besides, the mechanical properties of the composite were effectively enhanced by the formation of in situ second phases. The Vickers hardness and the fracture toughness of the composite reached 20.1 GPa and 5.8 MPa $m^{-1/2}$, respectively.

Advanced ceramics and protective coatings for high temperature applications have been recently attracted[1–11]. With a high melting point (about 3380 °C), high thermal and electrical conductivity, excellent strength at the severe environment, and brilliant thermal shock resistance, HfB_2 is one of the ultra-high temperature ceramics (UHTCs). Due to its excellent properties, it has been considered for high-temperature applications such as nose cone and the leading edge of hypersonic flight vehicles and advanced rocket motors[12–14]. Recently, many studies have been undertaken to densify HfB_2[15–17]. Because of the low self-diffusion coefficients and tightly covalent bonding, generally, pressure-assisted methods such as Spark plasma sintering (SPS), and Hot pressing (HP) are applied for consolidation of HfB_2-based composites. However, using these methods restrict geometrical dimensions, especially for complex-shaped specimens. Reactive pressureless sintering is one of the practical methods to fabricate near-net-shape HfB_2-based composites where matrix or reinforcement phases are in situ formed.

Brochu et al.[18] densified ZrB_2 ceramic by reactive pressureless sintering method using Zr and B powders as starting materials. However, they did not use any additive for the densification of ZrB_2; the maximum density was reported about 79% for monolithic ZrB_2.

Wang et al.[19] reported the relative density of 97.2% for B_4C–SiC–TiB_2 composite fabricated by reactive pressureless sintering method.

Zhang et al.[20] fabricated $Ta_{0.8}Hf_{0.2}C$–SiC composite using $HfSi_2$, TaC, and carbon black powders by reactive pressureless sintering method at 2200 °C. The relative density of the composite was reported about 99%.

It has been reported that the oxide impurities (HfO_2, B_2O_3) of HfB_2 starting powder can prevent the densification of HfB_2 ceramic[21]. Therefore, removing the oxide impurities and reaching full dense HfB_2-based composites has been a challenging issue for researchers. Some additives or reinforcements have been suggested to enhance the sinterability and mechanical properties of UHTCs. In an attempt to increase the sintered density of UHTC-based composites, some researchers used oxide and non-oxide additives such as Y_2O_3[22], Ta[23], Al[24], $TaSi_2$[25], and $MoSi_2$[26]. Among them, SiC is an additive that has been commonly used due to its capability to improve the mechanical properties as well as the oxidation resistance of transition metal borides[27,28]. Moreover, silicides have been added to HfB_2 to improve its mechanical properties owing to such superior properties as excellent creep resistance and oxidation behavior.

The addition of VSi_2 for enhancing properties of UHTC is a novel idea. However, the sintering process of HfB_2 ceramic with other silicides has been accomplished by other researchers. For example, Sciti et al.[25] densified

[1]Department of Materials Science and Engineering, Tarbiat Modares University, PO Box 14115-143, Tehran, Iran. [2]School of Metallurgy and Materials, College of Engineering, University of Tehran, Tehran, Iran. ✉email: S.ghadami@modares.ac.ir

Row material	Purity (%)	Mean particle size (μm)	Impurities	Vendor
HfB_2	95	20	HfO_2	Beijing Cerametek Materials (China)
VC	99.9	2	–	Merck (Germany)
Si	99.5	10	–	Merck (Germany)

Table 1. Specification of the starting powders before sintering.

SiC (vol%)	VSi_2 (vol%)	Temperature/ Vacuum pressure/ Dwell time of Reactive pressureless sintering process (°C/mbar/h)	Relative green density (%)	Relative density (%)	Elastic modulus (GPa)	Vickers Hardness (GPa)	Matrix Grain Size (μm)	Fracture Toughness (MPa $m^{1/2}$)
10	20	2150/0.05/4	60	98	401.3 ± 1.3	20.1 ± 1.1	10	5.8 ± 0.33

Table 2. Sintering conditions and properties of HfB_2–SiC–VSi_2 composite.

UHTC-based composites containing 3 vol% silicides of molybdenum or tantalum as sintering additives. They have reached the fracture toughness of 5.1 MPa $m^{1/2}$ for the HfB_2–$TaSi_2$ composites as well as 4.4 MPa $m^{1/2}$ for the HfB_2–$MoSi_2$ composites. In other research, Zhang et al.[29] fabricated ZrB_2–WSi_2 composite via hot pressing method. They reported the fracture toughness of 3.5 MPa $m^{1/2}$ for the composite. SiC and VSi_2 could be suitable additives for HfB_2-based composites, due to their low density, high thermal conductivity, and excellent oxidation and creep resistance[30,31].

The aim of this work is the fabrication and properties evaluation of HfB_2–SiC–VSi_2 composite which is fabricated by HfB_2, VC, and Si powders via reactive pressureless sintering method. We investigate the effect of in situ VSi_2 and SiC phases on the densification, microstructure, and mechanical properties of HfB_2–SiC–VSi_2 composite.

Experimental methods

In order to fabricate the HfB_2–15 vol%SiC–15vol%VSi_2 composite, the commercial HfB_2, VC, and Si powders were used as starting materials. The characteristics of starting powders are listed in Table 1. Calculations of volume fractions were performed to define the composition of the composite. The powders were milled by a high-energy planetary mill for 5 h in ethanol medium. WC–Co cup and balls were selected and a speed ratio of the milling process was defined 300 rpm. The weight ratio of powders to balls was determined 1:3. For removing ethanol from mixed powders, the drying process was accomplished for 24 h in air. Cylindrical specimens ($\Phi 25 \times 8$ mm^2) without any binders were cold-pressed by uniaxial pressing at 50 MPa and then were cold isostatically pressed at 300 MPa. Reactive pressureless sintering process was performed in a commercial graphite resistance heating furnace at 2150 °C for 4 h under a vacuum atmosphere of 0.05 mbar. For completing the formation of in situ phases, a heating rate was decreased from 1150 to 1350 °C according to the reaction (3). Table 2 shows the main features and the sintering conditions for the sintered composite.

Before the sintering process, the green density of the composite was measured by the ratio between the mass and the volume of the sintered specimens according to dimensional measurements. It should be noted that the relative green density was reported by the ratio between green and theoretical densities. The theoretical density of the composite was calculated based on the final composition after the sintering process (see Sect. Densification and microstructure and Fig. 2) by the rule of mixture according to theoretical densities of 11.2 g/cm^3 for HfB_2, 3.2 g/cm^3 for SiC, 4.42 g/cm^3 for VSi_2, and 12.2 g/cm^3 for HfC. The bulk density of sintered samples was measured using Archimedes method. Hence, the relative density of the sintered specimens was reported by the ratio between the bulk and theoretical densities. Young's modulus was determined through ultrasonic testing at 25 °C according to the ASTM C1198[32] by sound velocity using the TC600 model thickness measuring apparatus. The Vickers hardness test was carried out on the polished surfaces of the sintered specimens by a Vickers indenter with 0.3 kg applied load for 10 s[33]:

$$Hv = 1.854\frac{P}{d^2} \tag{1}$$

where Hv is the Vickers hardness (GPa), P refers to the applied force for indentation (N), and d means the average diagonal length of indent (m).

The fracture toughness of the sintered specimens was calculated using Evans and Charles's equation[34]:

$$KIC = 0.16(c/a)^{-3/2}(Ha^{1/2}) \tag{2}$$

where *KIC* refers to the fracture toughness (MPa $m^{-1/2}$), H means Vickers hardness (GPa), *c* is the average half-length of the crack acquired in the tips of the Vickers marks (m), and *a* is the average half-length of indentation diagonal (m). The fracture toughness was evaluated by the applied load of 20 kg.

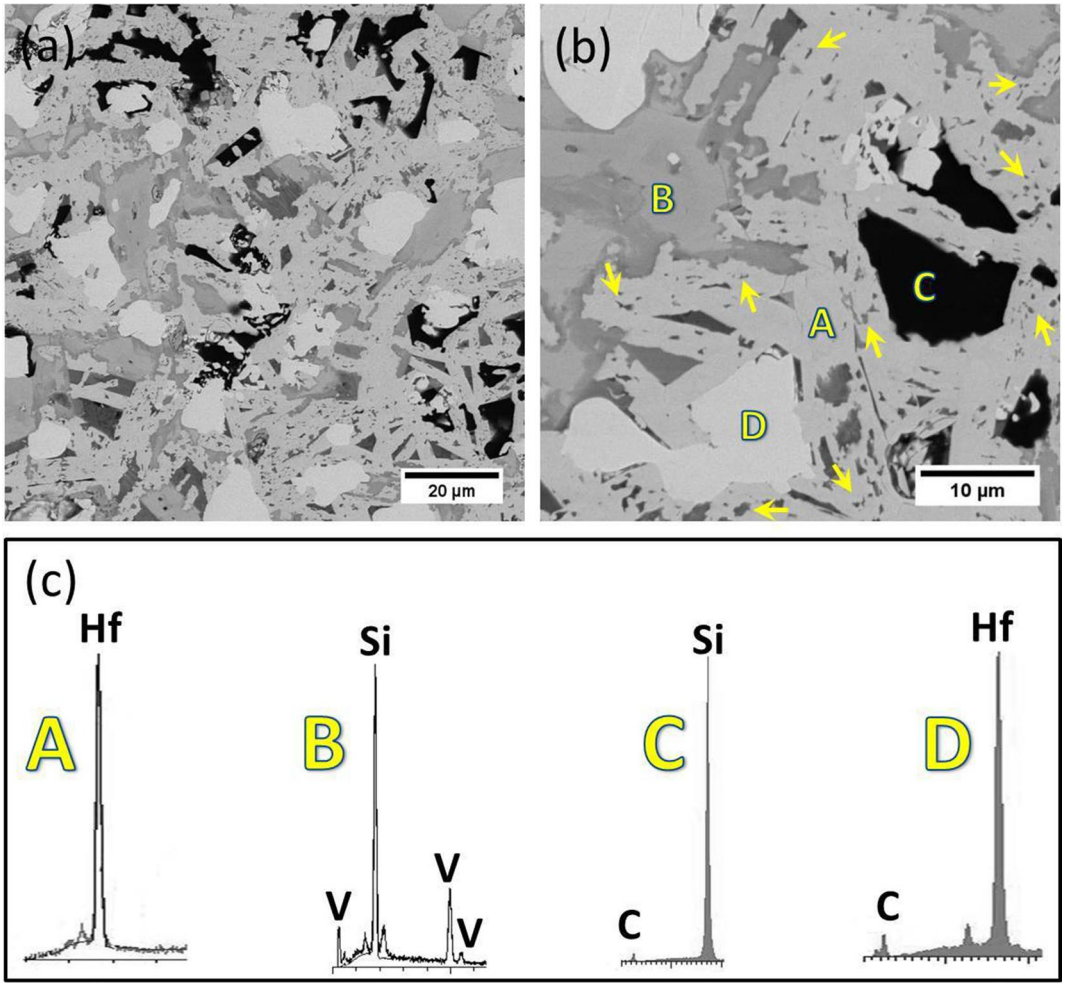

Figure 1. Field emission SEM micrographs of pressureless sintered HfB_2–SiC–VSi_2 composite at 2150 °C (**a**) low magnification, (**b**) high magnification, and (**c**) EDS patterns of spot A, spot B, spot C, and spot D. Ultra-fine grains indicated by arrows in (**b**) have chemical composition according to B.

To the accuracy of the result, five specimens for HfB_2–SiC–VSi_2 composite were tested and ten measurements were repeated for each specimen. Moreover, the microstructural observation was examined on the mirror-like surfaces of sintered specimens by field emission scanning electron microscope (FESEM, TESCAN, Model: MIRA3) equipped with energy-dispersive spectroscopy (EDS). Besides, to ensure reliable results, the microstructural analysis was done on different parts of the specimens. The phase composition was determined by X-ray diffraction analysis (XRD, Philips, Model: X'Pert MPD, Tube: Co, and λ: 1.78897 Å). The grain size of the sintered composite was estimated by the image analysis (ImageJ software). To determine the possibility of in situ formations of phases during the sintering process, thermodynamic calculations were performed using HSC software. The final composition after sintering was calculated by ImageJ analyzing software. For this purpose, ten random images of SEM micrographs at different magnifications were selected and evaluated.

Result and discussion

Densification and microstructure. The relative green and relative densities of reactive pressureless sintered HfB_2–SiC–VSi_2 composite are presented in Table 2. The relative density of the composite reached 98%. FESEM image of the microstructure of the pressureless sintered composite is shown in Fig. 1. It has been reported that diffusion rate and porosity mobility are enhanced by increasing the sintering temperature which finally causes the reduction of cavities in the sintered composite[35]. The very small amount of porosity is observed in the microstructure after the sintering process which confirms that the temperature of the sintering process (~2150 °C) was adequate to remove most of the porosities. On the other hand, the mobility of the grain boundary of HfB_2 was decreased by in situ formations of SiC and VSi_2 phases alongside HfB_2 grains. The average HfB_2 grain size was estimated about 10 µm. Some ultra-fine grains inside HfB_2 phase could be found and EDS analysis revealed them to be VSi_2. Due to the 1677 °C melting point of VSi_2, it seems that the VSi_2 was molten during the sintering process. The molten VSi_2 flowed through the capillaries and filled the pores. Based on this scenario, these ultra-fine grains were recrystallized VSi_2 which were located at pores and finally led to an improvement in the density of the composite. Aside from VSi_2 phase, three regions are distinguished in the microstructure of

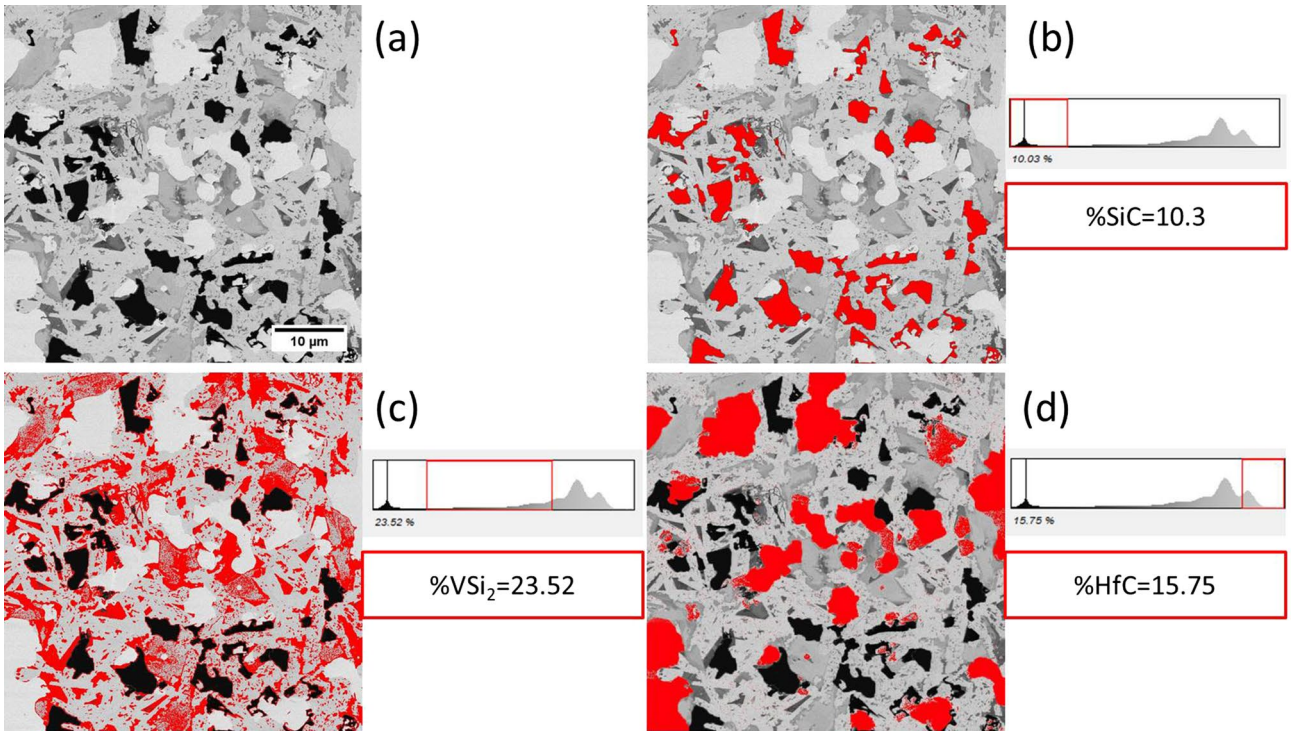

Figure 2. Estimated chemical composition of the pressureless sintered composite by ImageJ software. (**a**) the analyzed micrograph of HfB_2–SiC–VSi_2-composite, (**b**) estimated composition of SiC to 10.3%, (**c**) estimated composition of VSi_2 to 23.52%, and (**d**) estimated composition of HfC to 15.75%.

the composite. Black regions are SiC, white regions are HfC, and the light regions are HfB_2 according to EDS analysis. This result is in excellent agreement with the previous study of the fabrication of in situ HfB_2-based composites[21].

Figure 2 shows the final composition of the composite after the sintering process. The final composition of the composite was estimated HfB_2–10.3%SiC–20.52%VSi_2–15.75%HfC by image analysis which is close to the target composition.

Mechanical properties. The values of the Vickers hardness, the elastic modulus, and the fracture toughness of the composite are listed in Table 2. Owning to the hardness value of SiC (~ 27 GPa)[36] and HfC (~ 28 GPa)[37], the average hardness of the reactive pressureless sintered composite reached 20.1 GPa. However, the hardness value of VSi_2 is lower than HfB_2 matrix; in situ VSi_2 phase formation improved the hardness by promoting the elimination of porosities.

Sonber et al.[38] fabricated HfB_2–$TiSi_2$ composite by hot pressing method. They reported the hardness value of 11.5 GPa for monolithic HfB_2 and 25.4 GPa for HfB_2–$TiSi_2$ composite.

Ghadami et al.[21] demonstrated that the Vickers hardness of HfB_2-based composite improves with the in situ formation of SiC and $MoSi_2$ during sintering. They reported the hardness value of 18 GPa for monolithic HfB_2 and 25.2 GPa for HfB_2–SiC–$MoSi_2$ composite. Improvement of density by the formation in situ phases as well as the inherent hardness of in situ phases contributed to the desirable Vickers hardness of the composite.

Young's modulus of the composite was 401.3 GPa in which was close to the estimated Young's modulus using the role of mixture (about 424.7 GPa). According to Fig. 3, to evaluate the fracture toughness of the composite, the average half-length of the cracks was measured 45 μm and the average half-length of indentation diagonal was measured 108 μm.

The fracture toughness of the composite was measured to be 5.8 MPa $m^{-1/2}$ which was noticeably higher than those of the reported HfB_2-based composites in the range of 3.5–3.9 MPa $m^{-1/2}$[39,40]. The main reason for desirable fracture toughness was attributed to increasing obstacles for crack propagation by in situ formations of VSi_2 and SiC. HfB_2 large grain size (~ 10 μm) could also increase the fracture toughness. Figure 4 shows the crack propagation in the microstructure of the composite.

Because of a significant mismatch between the thermal expansion coefficient of HfB_2 (6.3×10^{-6} K^{-1})[41], SiC (4.7×10^{-6} K^{-1})[42], VSi_2 ($11.2–14.65 \times 10^{-6}$ K^{-1})[43], and HfC (6.6×10^{-6} K^{-1})[44], some compressive stresses may be induced after the sintering process. Therefore, the SiC particles are under compressive stress. On the other side, HfB_2 matrix is under tensile stress in a tangential direction as well as compressive stress in a radial direction. The compressive stress around SiC particles causes the crack is deflected. It should be concluded that the crack is deflected when the crack strikes SiC particle. SiC particle dissipates the energy of the crack resulting in enhancing the fracture toughness of the composite.

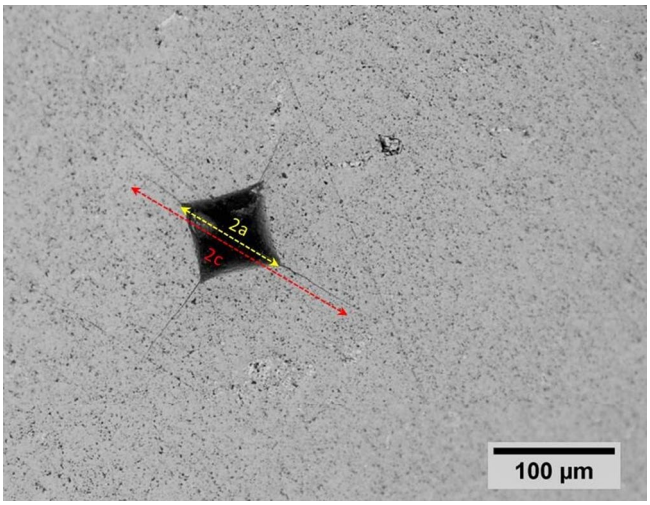

Figure 3. Optical microscope image of Vickers indentation for HfB_2–SiC–VSi_2 composite. Lengths of parameters a and b are shown based on Eq. (2).

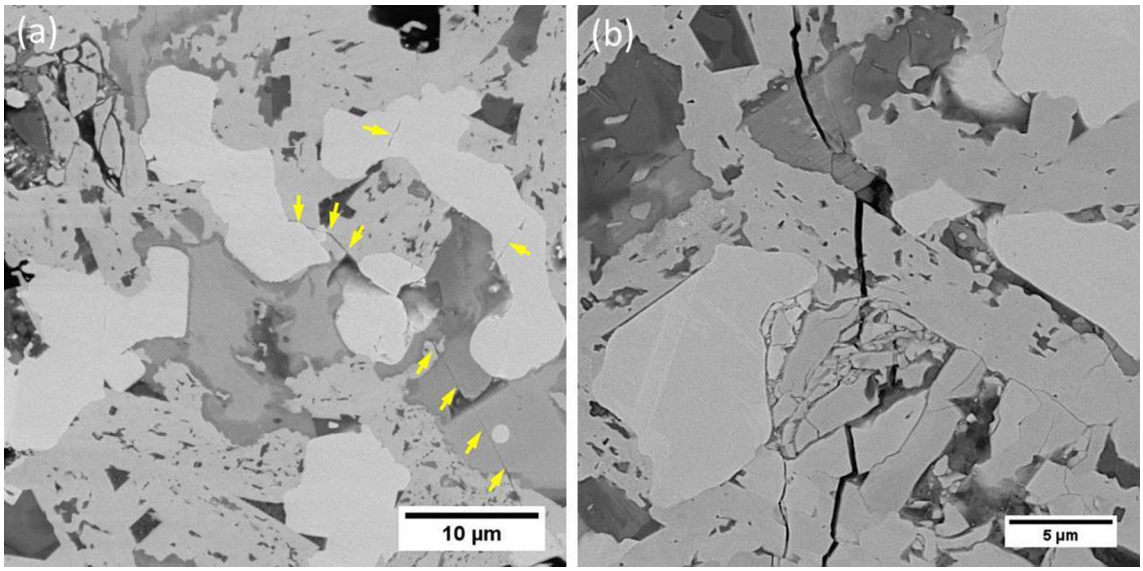

Figure 4. Backscattered image of indented crack propagation of HfB_2–SiC–VSi_2 composite. (**a**) low magnificent, the crack propagation is shown in yellow arrows and (**b**) high magnificent.

Hence, increasing compressive stresses around SiC particles enhanced the fracture toughness of HfB_2–SiC–VSi_2 composite. These results were supported by other researchers[45–49].

In previous studies, the effective role of reinforcement morphology was demonstrated[21,50].

The SiC particles were elongated and homogeneously distributed in the HfB_2 skeleton.

Besides, in situ formations of needle-like SiC particles provided more obstacles against the crack propagation. Padture et al.[51] reported that the elongated SiC grains enhance the fracture resistance by crack bridging and crack deflecting.

Figure 5 shows the interaction between in situ SiC particle and the crack. When the growth path of the crack tip strikes the SiC particle, three mechanisms may occur. First mechanism: the energy of the crack is not enough to break the SiC particle, but the crack has enough energy to change its growth direction. Therefore, the crack is deflected through the weaker direction (Fig. 5a). Second mechanism: in situ elongated SiC particle dissipates the crack energy by crack bridging mechanism (Fig. 5b). Third mechanism: SiC particle absorbs the whole energy of the crack and then the crack is pinned (Fig. 5c).

As a result, the formation of elongated α-SiC particles contributed to the favorable fracture toughness of the reactive pressureless sintered composite.

Figure 6 presents the fractured surface of the composite. As can be seen, in some areas the fracture surface is rough whereas in other areas the fracture surface is sharp and grains are pulled out. The sharp edges and pulled

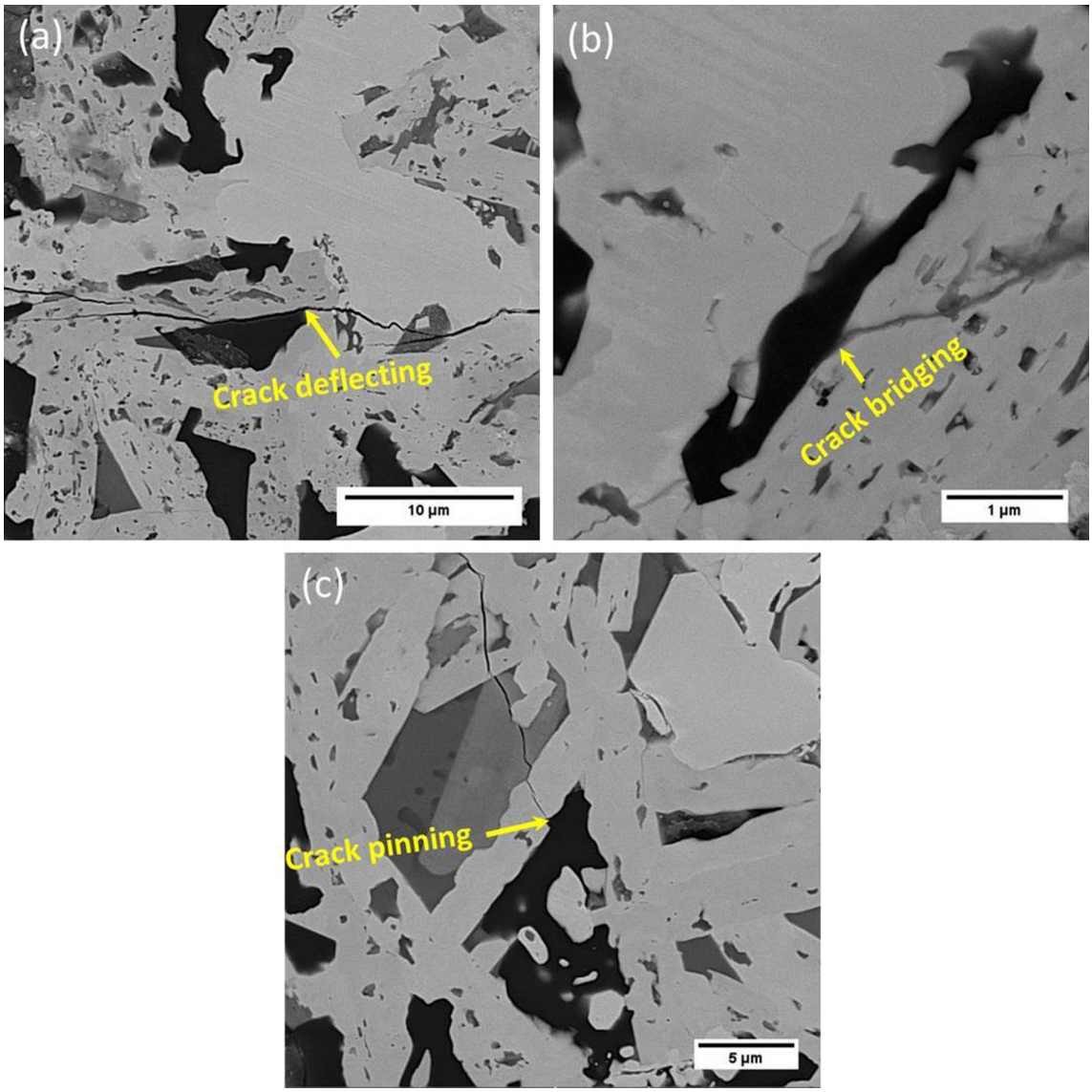

Figure 5. Toughening mechanism of the sintered composite. (**a**) Crack deflection, (**b**) crack bridging, and (**c**) crack pinning.

out grains prove that the crack propagates through the grain boundaries and leads to the inter-granular fracture mode. On the other side, the rough surfaces indicate that the grain boundaries are much more stronger than the inside of grains. The crack propagates through the inside of grains and leads to the intra-granular fracture mode.

This result proves that the fracture mode was mixed with inter- and intra-granular modes.

In situ formation of SiC and VSi_2 reinforcement particles contributed to improving the strength of grain boundaries and finally enhanced the fracture toughness of the composite.

In situ phase formation. Figure 7 illustrates the diagram of reaction possibility between VC and Si which was simulated according to the sintering condition (~0.05 mbar) by HSC software. VC and Si could react with each other and produce VSi_2 and SiC simultaneously. According to the thermodynamic calculations, VSi_2 and SiC could be formed even at the room temperature and the reaction (3) could happen at the beginning stages of the sintering process as following:

$$VC + 3Si = SiC + VSi_2 \quad (3)$$

However, it seems that the required kinetic energy for activation of the reaction (3) is not adequate at the initial temperatures. Ko et al.[52] demonstrated that SiC and VSi_2 could be formed at 1250 °C under argon atmosphere. Hence, the formation of SiC and VSi_2 needs higher temperatures (at least 1250 °C).

On the other side, VSi_2 and SiC decompose at 1350 °C and 1800 °C, respectively. However, the kinetic energy of the reverse direction of the reaction (3) is not sufficiently adequate. Hence, the decomposition of VSi_2 and SiC

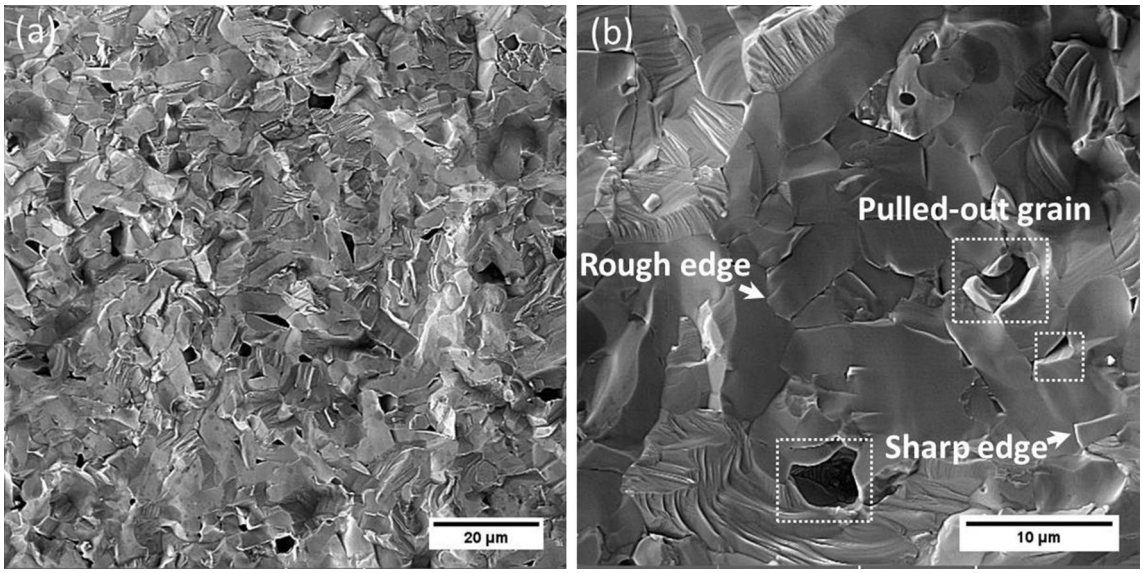

Figure 6. SEM fractographic of the composite. (**a**) low magnificent and (**b**) high magnificent. The presence of rough and sharp edges as well as pulled-out grains prove the mix of inter- and intra-granular fracture mode.

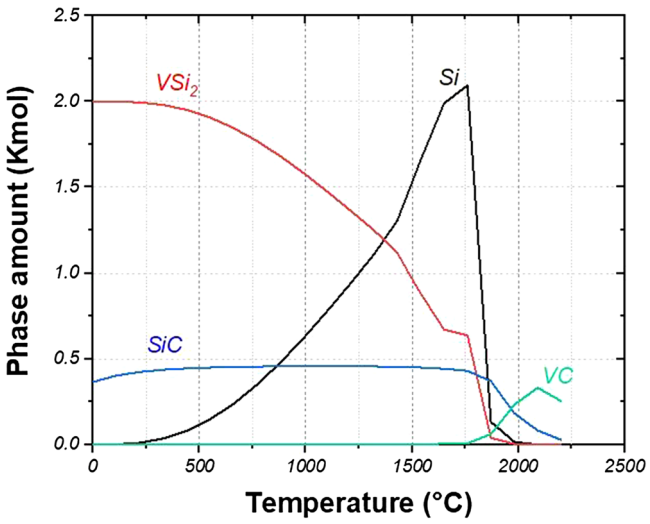

Figure 7. Calculated multiphase equilibrium by HSC software for in situ formation of SiC and VSi_2 reinforcement phases according to the sintering condition (VC = 1 kmol, Si = 3 kmol, and P ~ 0.05 mbar).

did not take place under the present sintering conditions (see Sect. 3.1). It leads to the conclusion that in situ VSi_2 and SiC phases could be mostly formed at 1250 °C with ΔG of − 92.793 kJ.

Shahedi Asl et al.[53] reported that the reaction between VC and ZrB_2 could be possible according to the following reaction:

$$ZrB_2 + VC = VB_2 + ZrC \quad (4)$$

Similarly, there is a chance to the reaction between HfB_2 and VC as following:

$$HfB_2 + VC = VB_2 + HfC \quad (5)$$

To find out the possibility of the reaction between HfB_2 and VC, thermodynamic calculations were performed for the reaction (5). Figure 8 illustrates the priority between reactions (3) and (5). With a larger negative delta G for the reaction (3), the reaction (3) is progressed predominantly. Therefore, the formation of VB_2 and HfC phases from the reaction (5) is unlikely to happen. Back to the details of the reaction (3), SiC and VSi_2 were completely formed at 1250 °C. In the temperature range of 1400–1700 °C delta G of this reaction was dramatically increased which indicated that a thermodynamic transformation could occur. It was reported that the melting points of SiC and VSi_2 are to be 2830 °C and 1677 °C, respectively[54,55]. It seems that the endothermic transformation is related to the melting of VSi_2. Based on this hypothesis, the melting process of VSi_2 was thoroughly completed

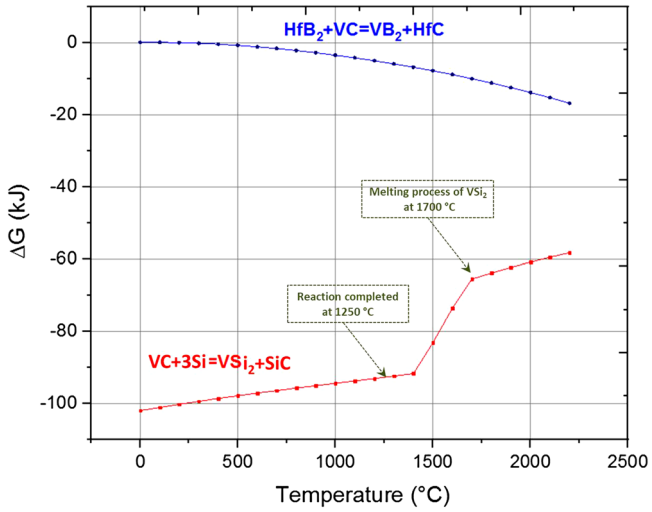

Figure 8. Standard Gibbs free energy of reactions between VC/Si and HfB_2/VC as a function of temperature at standard state (P ~ 1 atm).

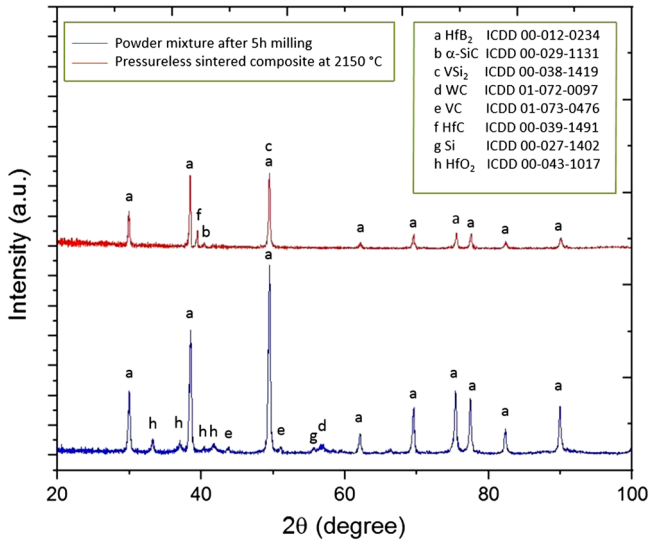

Figure 9. XRD patterns of mixed powders after 5 h milling process and HfB_2–SiC–VSi_2 composite by reactive pressureless sintering at 2150 °C.

at 1700 °C. This result was supported by the extracted result from the microstructural study. Moreover, in situ HfC phase could be formed according to the following reaction:

$$HfO_2 + 3WC = HfC + 3W + 2CO\,(g) \tag{6}$$

The mass of the WC impurity from milling media was measured which indicated that ~ 5 wt%WC was incorporated into the mixed powders. It has been reported that the located HfO_2 on the surface of HfB_2 powders plays a barrier role against densification[21]. WC impurity from milling media could react with HfO_2 from starting powder; hence, it could remove the oxide-impurity and finally enhance the sintering process.

Phase analysis. X-ray diffraction patterns of the mixed powders and the pressureless sintered composite are shown in Fig. 9. From this Fig. 9, HfB_2, HfO_2, VC, Si, WC phases were detected which indicate that HfO_2 and WC impurities were present in the starting mixtures. Owing to WC–Co cup and balls, 5 wt%WC could be inserted by the milling process. Besides, HfB_2 powder contained HfO_2 impurity based on Table 1. On the other hand, HfB_2, VSi_2, SiC, and HfC phases were found and no obvious impurity phases can be seen after the sinter-

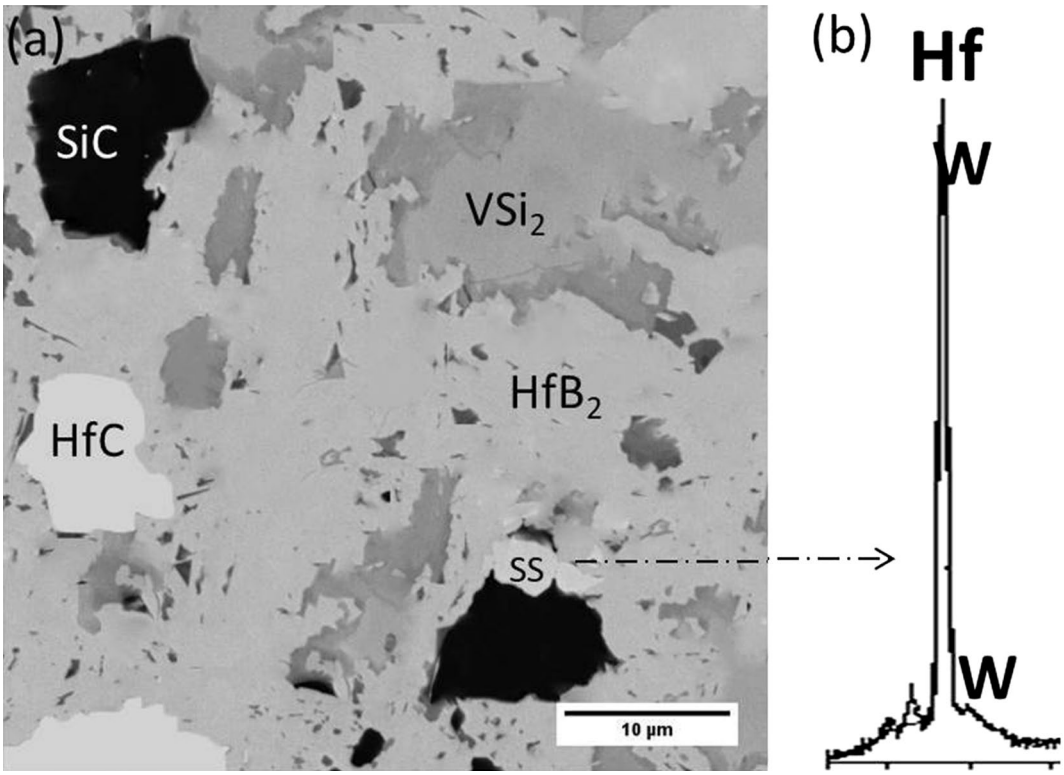

Figure 10. (**a**) Back-scattered electron image of HfB_2–SiC–VSi_2-composite and (**b**) corresponding EDS analysis showing the formation of (Hf, W)-B solid solution.

ing process. According to the reaction (6), it could be concluded that HfO_2 and WC reacted to each other and produced HfC. This result is supported by other researchers[56,57].

It has been reported that carbon could be penetrated from graphite mold to the structure of HfB_2-based composite during the sintering process[21,58]. Penetrated carbon could react with HfO_2 impurities at the temperature of 1700 °C according to the following reaction:

$$HfO_2 + 3C = HfC + 2CO(g) \quad (7)$$

It should be noted that the reaction (7) as well as the reaction (6) could produce HfC. However, this work intended to fabricate HfB_2-15vol% SiC-15 vol%VSi_2 composite, based on the reactions (6 and 7), HfC could be formed and the final composition included HfC according to Fig. 2.

Moreover, no corresponding peaks of vanadium carbide and silicon were identified after the sintering process.

The presence of VSi_2 and SiC peaks in Fig. 9 demonstrated that the reaction (3) was mostly completed. VB_2 phase was not detected after the sintering process which indicated that the reaction (5) was not favorable. On the other side, HfC phase was possibly formed from the reactions (6 and 7) and less likely from the reaction (5). W phase from the reaction (6) was not detected by XRD analysis.

It seems that W atoms were hosted in HfB_2 structure and led to the formation of (Hf, W)-B solid solution. However, detecting the negligible (Hf, W)-B solid solution needs to have more precise microstructural studies such as TEM technique. In this work, (Hf, W)-B solid solution was identified by EDS analysis as shown in Fig. 10. This hypothesis shows an excellent agreement with the reported result from other researchers[56,59–63].

Finally, Fig. 11 schematically illustrates the sintering mechanism of HfB_2–SiC–VSi_2 composite during the sintering process up to 2150 °C. After the milling process, mixed powders including HfB_2, Si, and VC are randomly distributed (Fig. 11a). During the sintering process, the reaction between Si and VC could happen at 1250 °C. Therefore, VSi_2 and SiC are formed as byproducts from reaction (3). Similarly, HfC, W, and CO(g) are formed from reaction (6 and 7) (Fig. 11b). CO gas product can release from the skeleton when HfC remains in the microstructure of the composite. W atoms from reaction (6) are hosted in HfB_2 structure and cause to the formation of (Hf, W)-B solid solution (Fig. 11c). VSi_2 is melted at 1700 °C and then molten VSi_2 flows through the capillaries and fills pores (Fig. 11d). Eventually, the microstructure consists of HfB_2, VSi_2, SiC, and HfC phases which distribute in the microstructure after the sintering process at 2150 °C (Fig. 11e).

Conclusions

HfB_2–SiC–VSi_2 composite was densified by reactive pressureless sintering using HfB_2, VC, and Si as starting powders at 2150 °C under vacuum atmosphere (0.05 mbar) for 4 h. Microstructural investigations and XRD analysis showed that in situ SiC and VSi_2 phases were formed during the sintering process and homogenously

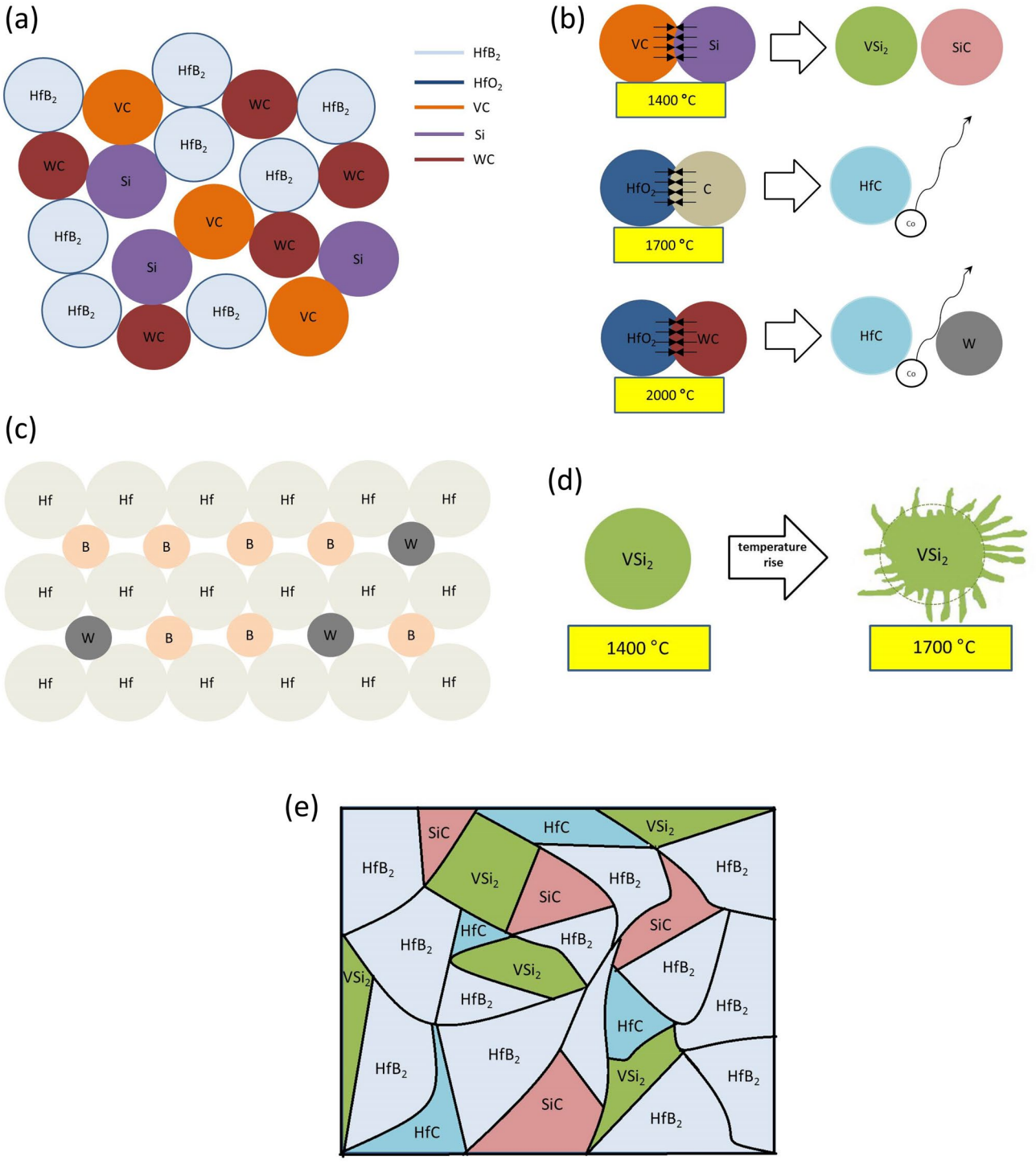

Figure 11. Schematic drawing of sintering mechanism during reactive consolidation of HfB_2–SiC–VSi_2 composite (**a**) random distribution of particles after 5 h milling process (**b**) reactions taking place during densification process (**c**) inter-substituting of W in HfB_2 structure and formation of (Hf, W)-B solid solution (**d**) melting process of VSi_2 at 1700 °C (**e**) final microstructure of the HfB_2–SiC–VSi_2 composite after sintering at 2150 °C.

distributed in HfB_2 skeleton. Moreover, HfO_2 impurity was successfully removed and turned to HfC by reacting with inserted WC impurity from milling media. The relative density of the composite was measured by 98%. According to thermodynamic calculations performed by HSC software, VSi_2 was melted at 1700 °C and filled pores which contributed to an increase in the relative density of the composite. The Young's modulus, Vickers hardness, and fracture toughness values of the composite were determined to be 401.3 GPa, 20.1 GPa,

and 5.8 MPa $m^{-1/2}$, respectively. The improvement of the mechanical properties of the sintered composite was attributed to the in situ formation of SiC and VSi_2 phases.

Received: 18 June 2020; Accepted: 15 September 2020
Published online: 06 October 2020

References

1. Sohi, M. H. & Ghadami, F. Comparative tribological study of air plasma sprayed WC–12% Co coating versus conventional hard chromium electrodeposit. *Tribol. Int.* **43**, 882–886 (2010).
2. Ghadami, F., Zakeri, A., Aghdam, A. S. R. & Tahmasebi, R. Structural characteristics and high-temperature oxidation behavior of HVOF sprayed nano-CeO_2 reinforced NiCoCrAlY nanocomposite coatings. *Surf. Coat. Technol.* **373**, 7–16 (2019).
3. Ghadami, F., Sohi, M. H. & Ghadami, S. Effect of TIG surface melting on structure and wear properties of air plasma-sprayed WC–Co coatings. *Surf. Coat. Technol.* **261**, 108–113 (2015).
4. Ghadami, F., Aghdam, A. S. R., Ghadami, S. & Zeng, Q. Effect of vacuum heat treatment on the oxidation kinetics of freestanding nanostructured NiCoCrAlY coatings deposited by high-velocity oxy-fuel spraying. *J. Vacuum Sci. Technol. A Vacuum Surfaces Films* **38**, 022601 (2020).
5. Ghadami, F. & Rouh Aghdam, A. S. Preparation of NiCrAlY/nano-CeO_2 powder with the core-shell structure using high-velocity oxy-fuel spraying process. *Mater. Chem. Phys.* **243**, 122551. https://doi.org/10.1016/j.matchemphys.2019.122551 (2020).
6. Ghadami, F., Ghadami, S. & Abdollah-Pour, H. Structural and oxidation behavior of atmospheric heat treated plasma sprayed WC–Co coatings. *Vacuum* **94**, 64–68 (2013).
7. Ghadami, F., Aghdam, A. S. R., Zakeri, A., Saeedi, B. & Tahvili, P. Synergistic effect of CeO_2 and Al_2O_3 nanoparticle dispersion on the oxidation behavior of MCrAlY coatings deposited by HVOF. *Ceram. Int.* **46**, 4556–4567 (2020).
8. Ghadami, F., Aghdam, A. S. R. & Ghadami, S. Abrasive wear behavior of nano-ceria modified NiCoCrAlY coatings deposited by the high-velocity oxy-fuel process. *Mater. Res. Express* **6**, 1250d1256 (2020).
9. Ghadami, F. & Aghdam, A. S. R. Improvement of high velocity oxy-fuel spray coatings by thermal post-treatments: A critical review. *Thin Solid Films* **678**, 42–52 (2019).
10. Ghadami, F. & Aghdam, A. S. R. Preparation of NiCrAlY/nano-CeO_2 powder with the core-shell structure using high-velocity oxy-fuel spraying process. *Mater. Chem. Phys.* **243**, 122551 (2020).
11. Ghadami, S., Taheri-Nassaj, E., Baharvandi, H. R. & Ghadami, F. Effect of in situ SiC and $MoSi_2$ phases on the oxidation behavior of HfB_2-based composites. *Ceram. Int.* **46**, 20299–20305 (2020).
12. Savino, R., Fumo, M. D. S., Silvestroni, L. & Sciti, D. Arc-jet testing on HfB_2 and HfC-based ultra-high temperature ceramic materials. *J. Eur. Ceram. Soc.* **28**, 1899–1907 (2008).
13. Zhang, G.-J., Guo, W.-M., Ni, D.-W. & Kan, Y.-M. *Ultrahigh Temperature Ceramics (UHTCs) Based on ZrB2 and HfB2 Systems: Powder Synthesis,Densification and Mechanical Properties* 012041 (IOP Publishing).
14. Seetala, N. V. & Webb, M. T. *Spark Plasma Heat Treated ZrB2-SiC and HfB2-SiC Composites* 1176–1181 (Trans Tech Publ).
15. Zhang, Y., Tan, D. W., Guo, W. M., Wu, L. X., Sun, S. K., You, Y., Lin, H. T. & Wang, C. Y. Improvement of densification and microstructure of HfB2 ceramics by Ta/Ti substitution for Hf. J. Am. Ceram. Soc. **103**, 103–111 (2020).
16. Baharvandi, H. R. & Mashayekh, S. Effects of SiC content on the densification, microstructure and mechanical properties of HfB_2–SiC composites. *Int. J. Appl. Ceramic Technol.* **17**, 449–458 (2020).
17. Mashayekh, S. & Baharvandi, H. R. Effects of SiC or $MoSi_2$ second phase on the oxide layers structure of HfB_2-based composites. *Ceram. Int.* **43**, 15053–15059 (2017).
18. Brochu, M., Gauntt, B. D., Boyer, L. & Loehman, R. E. Pressureless reactive sintering of ZrB_2 ceramic. *J. Eur. Ceram. Soc.* **29**, 1493–1499 (2009).
19. Wang, S. *et al.* Preparing B_4C–SiC–TiB_2 composites via reactive pressureless sintering with B_4C and $TiSi_2$ as raw materials. *J. Mater. Res. Technol.* **9**, 8685–8696 (2020).
20. Zhang, B. *et al.* Harmonized toughening and strengthening in pressurelessly reactive-sintered $Ta_{0.8}Hf_{0.2}C$–SiC composite. *J. Eur. Ceramic Soc.* **38**, 5610–5614 (2018).
21. Ghadami, S., Taheri-Nassaj, E. & Baharvandi, H. R. Novel HfB_2–SiC–$MoSi_2$ composites by reactive spark plasma sintering. *J. Alloy. Compd.* **809**, 151705 (2019).
22. Zhang, X., Li, X., Han, J., Han, W. & Hong, C. Effects of Y_2O_3 on microstructure and mechanical properties of ZrB_2–SiC ceramics. *J. Alloy. Compd.* **465**, 506–511 (2008).
23. Opila, E., Levine, S. & Lorincz, J. Oxidation of ZrB_2- and HfB $_2$-based ultra-high temperature ceramics: Effect of Ta additions. *J. Mater. Sci.* **39**, 5969–5977 (2004).
24. Yi, H. C., Guigné, J. Y., Woodger, T. C. & Moore, J. J. Combustion synthesis of HfB 2-Al composites. *Metall. Mater. Trans. B* **29**, 877–887 (1998).
25. Sciti, D., Bonnefont, G., Fantozzi, G. & Silvestroni, L. Spark plasma sintering of HfB_2 with low additions of silicides of molybdenum and tantalum. *J. Eur. Ceram. Soc.* **30**, 3253–3258 (2010).
26. Sciti, D., Silvestroni, L. & Bellosi, A. Fabrication and properties of HfB_2–$MoSi_2$ composites produced by hot pressing and spark plasma sintering. *J. Mater. Res.* **21**, 1460–1466 (2006).
27. Sciti, D. & Silvestroni, L. Processing, sintering and oxidation behavior of SiC fibers reinforced ZrB_2 composites. *J. Eur. Ceram. Soc.* **32**, 1933–1940 (2012).
28. Han, J., Hu, P., Zhang, X. & Meng, S. Oxidation behavior of zirconium diboride–silicon carbide at 1800 °C. *Scripta Mater.* **57**, 825–828 (2007).
29. Zhang, H. B. *et al.* Preparation, texturing and mechanical properties of ZrB_2–WSi_2 ceramics via reactive hot pressing and hot forging. *Adv. Appl. Ceram.* **113**, 389–393 (2014).
30. Kelly, J. *The Scaled-Up Synthesis of Nanostructured Ultra-High-Temperature Ceramics and Resistance Sintering of Tantalum Carbide Nanopowders and Composites* (2013).
31. Kurokawa, K. & Yamauchi, A. *Classification of Oxidation Behavior of Disilicides* 227–232 (Trans Tech Publ).
32. ASTM C1198-20, Standard test method for dynamic Young's modulus, shear modulus, and Poisson's ratio for advanced ceramics by sonic resonance, ASTM International, West Conshohocken, PA (2020). https://www.astm.org.
33. Chicot, D. & Lesage, J. Absolute hardness of films and coatings. *Thin Solid Films* **254**, 123–130. https://doi.org/10.1016/0040-6090(94)06239-H (1995).
34. Evans, A. G. & Charles, E. A. Fracture toughness determinations by indentation. *J. Am. Ceram. Soc.* **59**, 371–372 (1976).
35. Khodaei, M., Yaghobizadeh, O., Ehsani, N., Baharvandi, H. R. & Dashti, A. The effect of TiO_2 additive on sinterability and properties of SiC–Al_2O_3–Y_2O_3 composite system. *Ceram. Int.* **44**, 16535–16542 (2018).
36. Namini, A. S. *et al.* Microstructural development and mechanical properties of hot pressed SiC reinforced TiB_2 based composite. *Int. J. Refract Metal Hard Mater.* **51**, 169–179 (2015).
37. Ni, D.-W., Liu, J.-X. & Zhang, G.-J. Microstructure refinement and mechanical properties improvement of HfB_2–SiC composites with the incorporation of HfC. *J. Eur. Ceram. Soc.* **32**, 2557–2563. https://doi.org/10.1016/j.jeurceramsoc.2012.02.017 (2012).

38. Sonber, J. K. *et al.* Investigations on synthesis of HfB_2 and development of a new composite with $TiSi_2$. *Int. J. Refract Metal Hard Mater.* **28**, 201–210. https://doi.org/10.1016/j.ijrmhm.2009.09.005 (2010).
39. Hu, C., Sakka, Y., Jang, B., Tanaka, H., Nishimura, T., Guo, S. & Grasso, S. Microstructure and properties of ZrB_2–SiC and HfB_2–SiC composites fabricated by spark plasma sintering (SPS) using $TaSi_2$ as sintering aid. *J. Ceram. Soc. Jpn.* **118**, 997–1001 (2010).
40. Bellosi, A., Monteverde, F. & Sciti, D. Fast densification of ultra-high-temperature ceramics by spark plasma sintering. *Int. J. Appl. Ceram. Technol.* **3**, 32–40 (2006).
41. Ni, D. W., Zhang, G. J., Kan, Y. M. & Wang, P. L. Hot pressed HfB2 and HfB_2–20 vol% SiC ceramics based on HfB_2 powder synthesized by borothermal reduction of HfO_2. *Int. J. Appl. Ceram. Technol.* **7**, 830–836 (2010).
42. Zou, J. *et al.* High-temperature bending strength, internal friction and stiffness of ZrB_2–20 vol% SiC ceramics. *J. Eur. Ceram. Soc.* **32**, 2519–2527 (2012).
43. Murarka, S. P. Refractory silicides for integrated circuits. *J. Vacuum Sci. Technol.* **17**, 775–792 (1980).
44. Gasch, M. J., Ellerby, D. T. & Johnson, S. M. *Handbook of Ceramic Composites* 197–224 (Springer, New York, 2005).
45. Ghadami, S., Baharvandi, H. R. & Ghadami, F. Influence of the vol% SiC on properties of pressureless Al_2O_3/SiC nanocomposites. *J. Compos. Mater.* **50**, 1367–1375 (2016).
46. Monteverde, F. Ultra-high temperature HfB_2–SiC ceramics consolidated by hot-pressing and spark plasma sintering. *J. Alloy. Compd.* **428**, 197–205 (2007).
47. Athanasiou, C.-E., Hongler, M.-O. & Bellouard, Y. Unraveling brittle-fracture statistics from intermittent patterns formed during femtosecond laser exposure. *Phys. Rev. Appl.* **8**, 054013 (2017).
48. Athanasiou, C. E., Zhang, H., Ramirez, C., Xi, J., Baba, T., Wang, X., Zhang, W., Padture, N. P., Szlufarska, I. & Sheldon, B. W. High toughness carbon-nanotube-reinforced ceramics via ion-beam engineering of interfaces. *Carbon* (2020).
49. Liu, X., Athanasiou, C. E., Padture, N. P., Sheldon, B. W. & Gao, H. A machine learning approach to fracture mechanics problems. *Acta Mater.* (2020).
50. Sayyadi-Shahraki, A., Rafiaei, S. M., Ghadami, S. & Nekouee, K. A. Densification and mechanical properties of spark plasma sintered Si_3N_4/ZrO_2 nano-composites. *J. Alloys Compd.* **776**, 798–806 (2019).
51. Padture, N. P. & Lawn, B. R. Toughness properties of a silicon carbide with an in situ induced heterogeneous grain structure. *J. Am. Ceram. Soc.* **77**, 2518–2522 (1994).
52. Ko, I.-Y., Park, J.-H., Yoon, J.-K., Doh, J.-M. & Shon, I.-J. Properties and synthesis of dense nanostructured VSi_2–SiC by high-frequency induction heated combustion. *Met. Mater. Int.* **16**, 219–223 (2010).
53. Asl, M. S., Nayebi, B., Ahmadi, Z., Parvizi, S. & Shokouhimehr, M. A novel ZrB_2–VB2–ZrC composite fabricated by reactive spark plasma sintering. *Mater. Sci. Eng. A* **731**, 131–139 (2018).
54. Kang, H.-K. & Kang, S. B. Thermal decomposition of silicon carbide in a plasma-sprayed Cu/SiC composite deposit. *Mater. Sci. Eng. A* **428**, 336–345 (2006).
55. Smith, J. F. The Si–V (silicon–vanadium) system: Addendum. *Bull. Alloy Phase Diagrams* **6**, 266–271 (1985).
56. Ni, D.-W., Liu, J.-X. & Zhang, G.-J. Pressureless sintering of HfB_2–SiC ceramics doped with WC. *J. Eur. Ceram. Soc.* **32**, 3627–3635 (2012).
57. Liu, J.-X. Zhang, G.-J., Xu, F.-F., Wu, W.-W., Liu, H.-T., Sakka, Y., Nishimura, T., Suzuki, T. S., Ni, D.-W. & Zou, J. Densification, microstructure evolution and mechanical properties of WC doped HfB_2–SiC ceramics. *J. Eur. Ceram. Soc.* **35**, 2707–2714 (2015).
58. Monteverde, F. & Bellosi, A. Microstructure and properties of an HfB_2-SiC composite for ultra high temperature applications. *Adv. Eng. Mater.* **6**, 331–336 (2004).
59. Hu, D.-L., Zheng, Q., Gu, H., Ni, D.-W. & Zhang, G.-J. Role of WC additive on reaction, solid-solution and densification in HfB_2–SiC ceramics. *J. Eur. Ceram. Soc.* **34**, 611–619 (2014).
60. Piriou, C. *et al.* Sintering and oxidation behavior of HfB_2–SiC composites from 0 to 30 vol% SiC between 1450 and 1800 K. *Ceram. Int.* **45**, 1846–1856. https://doi.org/10.1016/j.ceramint.2018.10.075 (2019).
61. Liu, J.-X. *et al.* Densification, microstructure evolution and mechanical properties of WC doped HfB_2–SiC ceramics. *J. Eur. Ceram. Soc.* **35**, 2707–2714. https://doi.org/10.1016/j.jeurceramsoc.2015.04.009 (2015).
62. Zou, J. *et al.* Chemical reactions, anisotropic grain growth and sintering mechanisms of self-reinforced ZrB_2–SiC doped with WC. *J. Am. Ceram. Soc.* **94**, 1575–1583 (2011).
63. Guo, S., Liu, T., Ping, D.-H. & Nishimura, T. Enhanced high-temperature strength of HfB_2–SiC composite up to 1600 °C. *J. Eur. Ceram. Soc.* **38**, 1152–1157. https://doi.org/10.1016/j.jeurceramsoc.2017.12.040 (2018).

Acknowledgements

The first author is very tankful of Mr. Mohammad Amin Davoudabadi for language editing of this article.

Author contributions

S.Ghadami: conceptualization, methodology, investigation, writing—original draft. E.Taheri-Nassaj: supervision, writing—review and editing. H.R.Baharvandi: supervision, writing—review and editing. F.Ghadami: methodology, investigation, writing—review and editing. All authors reviewed the manuscript.

Competing interests

The authors declare no competing interests.

Additional information

Correspondence and requests for materials should be addressed to S.G.

Reprints and permissions information is available at www.nature.com/reprints.

Publisher's note Springer Nature remains neutral with regard to jurisdictional claims in published maps and institutional affiliations.